A direct link between active matter and sheared granular systems

Peter K. Morse[a,1,2], Sudeshna Roy[b,c,1], Elisabeth Agoritsas[d,1], Ethan Stanifer[b,c], Eric I. Corwin[e,f], and M. Lisa Manning[b,c,2]

[a]Department of Chemistry, Duke University, Durham, NC 27710; [b]Department of Physics, Syracuse University, Syracuse, NY 13244; [c]BioInspired Institute, Syracuse University, Syracuse, NY 13244; [d]Institute of Physics, Ecole Polytechnique Fédérale de Lausanne, CH-1015 Lausanne, Switzerland; [e]Department of Physics, University of Oregon, Eugene, OR 97403; and [f]Materials Science Institute, University of Oregon, Eugene, OR 97403

The similarity in mechanical properties of dense active matter and sheared amorphous solids has been noted in recent years without a rigorous examination of the underlying mechanism. We develop a mean-field model that predicts that their critical behavior—as measured by their avalanche statistics—should be equivalent in infinite dimensions up to a rescaling factor that depends on the correlation length of the applied field. We test these predictions in two dimensions using a numerical protocol, termed "athermal quasistatic random displacement," and find that these mean-field predictions are surprisingly accurate in low dimensions. We identify a general class of perturbations that smoothly interpolates between the uncorrelated localized forces that occur in the high-persistence limit of dense active matter and system-spanning correlated displacements that occur under applied shear. These results suggest a universal framework for predicting flow, deformation, and failure in active and sheared disordered materials.

sheared granular matter | dense active matter | dynamical mean-field theory | energy landscapes | generalized rheology

The statistical physics of active matter—where energy is injected at the smallest scale, that of the particles themselves—is highly nontrivial, exhibiting new features such as giant number fluctuations and motility-induced phase separation (1, 2). While comprehensive theories have been developed for many of these phenomena at low and intermediate densities (2, 3), the behavior of highly dense, glassy active matter remains more mysterious. Recent work by Henkes et al. (4, 5) highlights the important role of the potential energy landscape in constraining and dictating the behavior of dense active matter, which is in some ways similar to the situation in glasses excited by thermal fluctuations. Nevertheless, work by Berthier et al. (6, 7) emphasizes important differences between the dynamics of thermal and active glasses within the glassy potential energy landscape. Therefore, the large body of work on thermally excited glasses cannot be transferred immediately to active glasses, and so a predictive theory for the dynamics of dense active matter remains elusive.

Meanwhile, the dynamics of athermal sheared disordered materials, where energy is injected at the largest scale, globally from the boundaries, have been the subject of intense study for decades. A recent breakthrough allows an exact analytic solution for the behavior of slowly sheared systems in infinite dimensions, where interactions are exactly mean field (8–14). These results qualitatively explain many features in sheared two- and three-dimensional glassy solids. Perhaps more interestingly, new work suggests that the dynamical mean-field equations in infinite dimensions have the same structure regardless of whether the driving forces are generated by global shear or active forces on each particle (6, 15–17), as all such forcing can be represented by memory kernels with the same functional form.

There is also evidence of similarities between sheared and active glassy systems in two- and three-dimensional simulations; recent studies have noted that in granular systems the two forc-ing mechanisms yield similar critical behavior (18), large density fluctuations (4, 19), effective temperatures (20), aging behavior (21), and Eshelby deformations (22).

What is missing in the low-dimensional scenarios is a unifying picture as developed in infinite dimensions; to develop such a picture, it is necessary to first examine how and where discrepancies between shear and random forces appear. For example, Liao and Xu (18) noted that self-propelled particles driven by constant forces with the same magnitude in random directions will have the same diverging viscosity as their sheared counterparts (23–25) when jamming is approached, albeit with different critical exponents. Moreover, the values of the exponents can be changed by altering features of the forces on the self-propelled particles. Therefore, one wonders whether there may be a family of forcing fields, including shear and different types of self-propulsion, where all of the resulting dynamics could be understood and predicted as part of a universal description of failure in jammed solids.

One hint about how such a framework might be constructed comes from the density of states that describes the spectrum of vibrational modes about a mechanically stable state in the potential energy landscape. More specifically, in low dimensions, it has been shown that the linear response of particles to either random forces in the limit of low rotational noise or long persistence length (4, 5, 26) or to shear (27) is dominated by the lowest eigenmode. Very close to an instability, this lowest eigenmode specifies the direction in the energy landscape with the lowest energy barrier (28) and highlights the direction in which particles must move to leave one mechanically stable state and find another (29, 30).

Significance

There is not yet a robust theoretical framework predicting the dynamics of dense active matter, where energy is injected at the scale of constituent particles. Previous work has shown that some features of dense active matter are similar to those in dense disordered materials that are sheared globally from the boundaries. Using analytic and computational tools, we show that there is a direct correspondence between active matter and applied shear strain, which can in turn be used to help predict the behavior of dense active matter.

PHYSICS

Taken together, these previous results suggest that in two-dimensional (2D) and three-dimensional (3D) materials there is a direct connection between how a disordered system traverses the energy landscape under shear and under random forces in the limit of zero rotational noise. Here we develop an exact infinite-dimensional mean-field theory prediction for the mechanical response of materials under shear and such active forces. We explicitly test this prediction by analyzing numerical simulations of soft spheres in two dimensions and comparing dynamics under athermal quasistatic shear (AQS) (30) and a constrained dynamics we term athermal quasistatic random displacements (AQRD).

One goal of this article is to establish AQRD as an interesting and important limit of active matter dynamics. In AQRD, each particle is displaced continuously along its own self-propelled direction. Typical active matter simulations study overdamped self-propelled particles that move under constant force or equivalently constant velocity when the damping is homogeneous (2, 3). The direction of self-propulsion changes on a timescale called the persistence time, which is parameterized by the rotational noise. Therefore, AQRD is similar to self-propelled particles in the limit where the rotational noise is zero and the self-propelled velocity is slower than any other relaxation process inside the material.

An important difference between the two is, however, that active particles move under constant force, whereas AQRD particles move at constant displacement. This is in direct analogy to two different kinds of rheology experiments: 1) those where a system is subject to a constant shear force at the boundary, called "creep" experiments, and 2) those where the material is subject to a constant velocity condition at the boundary, called "constant strain rate" experiments. AQS is the zero-strain rate limit of the latter. In this work, we focus on AQRD because simulations and experiments which control strain rate (or displacements) are known to be very useful for characterizing material properties, and so there are a large amount of data in the literature for comparison. We focus on the preyielding regime, corresponding with the "start-up" phase of a simulation or experiment where the response depends strongly on the initial preparation of the material and the infinite-dimensional mean-field equations are solvable (8–14, 31). In contrast, stress-controlled creep experiments are fundamentally limited because the system can cross only energy barriers which are surmountable by the fixed applied stress, and under slow driving they exhibit complicated discontinuous stick–slip dynamics (32, 33). Therefore, while our primary focus in this article is on AQRD dynamics, we also introduce and study athermal quasistatic random force (AQRF) simulations, which are the random equivalent to creep experiments, and demonstrate that AQRF and AQRD are equivalent in linear response.

We next proceed to show that under shear (AQS) and random displacements (AQRD), scaling relations describing the avalanche statistics and the sampling of saddle points are identical and consistent with mean-field predictions, although the prefactors differ. We hypothesize that differences in those prefactors, including the shear modulus, are governed by the correlation length scale associated with the imposed displacement field; in shear this length is the size of the box, while for completely random fields it is the size of individual particles. In addition, the mean-field calculation predicts that these prefactors are precisely determined by the distribution of the imposed displacement field, which in turn causes fluctuations in strain between nearby particles.

Therefore, we systematically vary this correlation length in our simulations and find that the coefficients exhibit a systematic power-law scaling that matches mean-field predictions. We also study the effect of material preparation on these results, demonstrating that shear and random displacement fields are similar even in ultrastable glasses.

Taken together, this demonstrates that shear can be considered as a highly correlated special case of more general random displacements and establishes AQRD as a useful and interesting limit of active matter with a direct link to sheared systems.

Methods

Two Ways of Traversing the Energy Landscape. When constructing the energy landscape of allowed configurations, there are two types of variables that play a priori different roles: State variables are explicitly specified by the experimental or simulation protocol, while reaction coordinates are free to vary under constraints imposed by state variables. For instance, a standard infinite-temperature quench (34) considers shear strain to be a state variable during preparation, while shear-stabilization methods (35) treat strain as a reaction coordinate during preparation, regardless of how the strain variable is used afterward. Therefore, the use of strain or the box degrees of freedom as state variables is merely an artifact of the way in which experiments or simulations are performed. Moreover, during an athermal quasistatic perturbation, we adjust a state variable and then reminimize the system by allowing all reaction coordinates to find their nearest local energy minima.

An applied shear strain, illustrated by the red arrows in Fig. 1A, perturbs the system in its potential energy landscape. One way to represent this perturbation is to view the landscape as a function of the Nd reaction coordinates (particle positions), so that adjusting the state variable (the magnitude of strain under simple shear) contorts the landscape in that Nd-dimensional space (29, 30, 35). As a system is sheared toward a saddle point, a nearby energy barrier is lowered until the system reaches the saddle point and moves downhill toward a new minimum.

It is equivalent to describe this process instead as moving in an $Nd + 1$-dimensional landscape where we explicitly push the system along the box degree of freedom; i.e., we control the state variable corresponding to the magnitude of simple shear strain, as shown in Fig. 1B. In this framework, there are two types of saddle points: those parallel to the strain state variable and those perpendicular to it. The ones perpendicular to the strain are the same as the saddles in the Nd-dimensional representation, whereas the saddles parallel to the strain correspond to the shear modulus changing sign, which does not correspond to an instability in a strain-controlled measurement (36).

A second type of possible perturbation is a random displacement field, where we choose a random direction in configuration space $|c\rangle$ and promote it to a controlled state variable. An example field $|c\rangle$ is illustrated by the red arrows in Fig. 1D. Thus, after perturbing along $|c\rangle$, the system is free to relax along all directions perpendicular to $|c\rangle$, but motion along $|c\rangle$ is restricted via constrained minimization to the other $Nd - 1$ dimensions. The saddles encountered in such dynamics are thus always perpendicular to $|c\rangle$, and we ask whether the distribution of saddles and their corresponding stress drops follow the same distribution as those encountered under shear strain.

Numerical Model Description. We simulate N Hertzian spheres in $d = 2$ dimensions where N is the number of particles. Except where specified when using ultrastable glasses, our systems are a 50:50 mixture of bidisperse disks with diameter ratio 1:1.4 to avoid crystallization. For the pressure sweep data, we prepare our systems at a target pressure by performing a standard infinite-temperature quench (34), followed by FIRE (Fast Inertial Relaxation Engine) minimization (37) at a packing fraction such that we stay above the target pressure, followed by a careful decompression (36, 38). For the correlation length sweep, we prepare our systems at a pressure of $p = 0.0236 \pm 0.0004$ via simple infinite-temperature quench at a packing fraction $\phi = 0.94$ (34). In each case, we use the Hertzian contact potential
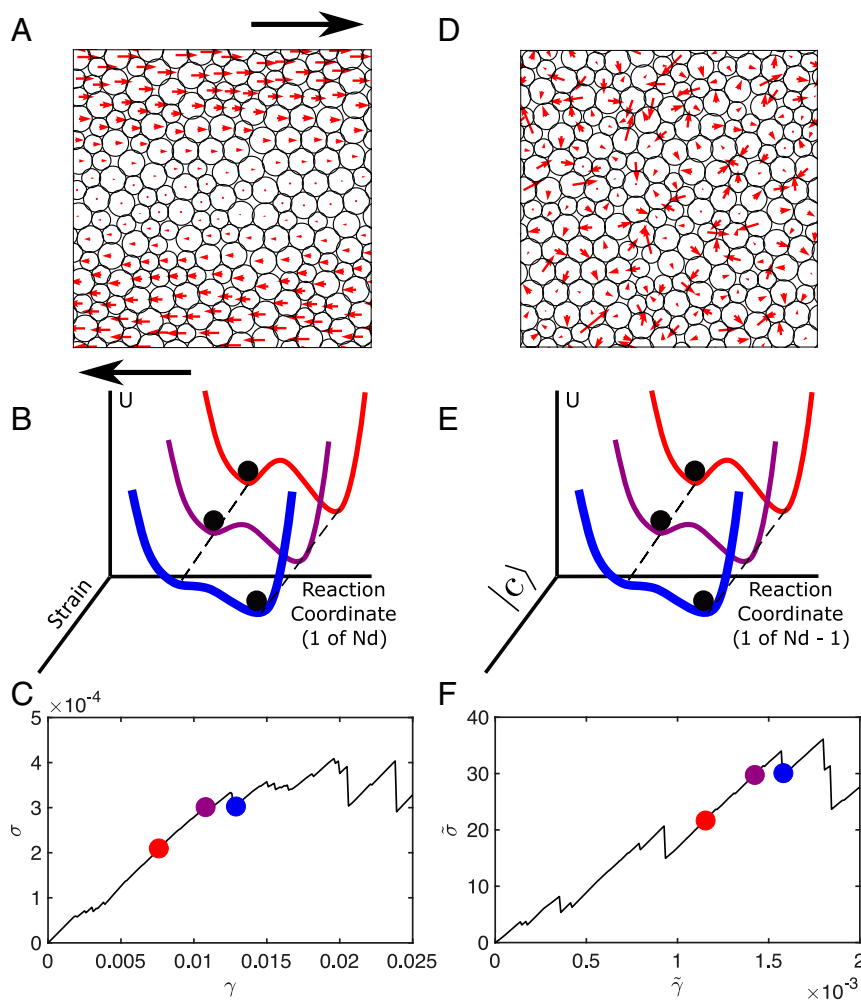
Fig. 1. Two methods of traversing the energy landscape: AQS and AQRD. (*A*) Forces applied to particles in an AQS ensemble. (*B*) Potential energy landscape splitting out the $Nd + 1$ degrees of freedom into Nd (one of which is the reaction coordinate shown) and strain. (*C*) Stress–strain curve showing that stress drop occurs when a saddle point in the reaction coordinate is reached by traversing along the strain coordinate. (*D*) Forces applied to particles in a sample AQRD ensemble. (*E*) Potential energy landscape splitting out the Nd degrees of freedom (for fixed box shape) into $Nd - 1$ (one of which is the reaction coordinate shown) and the vector along which random displacements are applied. (*F*) Random-stress vs. random-strain curve showing that random-stress drop occurs when a saddle point in the reaction coordinate is reached by traversing along the $|c\rangle$ coordinate. Highlighted points in *C* and *F* correspond with the curve of matching color in *B* and *E*, respectively.

$$U = \frac{1}{5/2} \sum_{ij} \Theta(\varepsilon_{ij}) \varepsilon_{ij}^{5/2}, \qquad [1]$$

where Θ is the Heaviside function, $\varepsilon_{ij} = 1 - r_{ij}/(\rho_i + \rho_j)$ is the dimensionless overlap, ρ_i is the radius of particle i, and r_{ij} is the distance between particles i and j. All length scales are reported in natural units of the minimum particle diameter.

Athermal Quasistatic Shear. Under the now-standard method of AQS (30), our system of particles is subject to simple shear via Lees–Edwards boundary conditions where the periodic replicas in the y direction are shifted by an amount γL_y in the x direction, and γ is the magnitude of simple shear which is the only nonzero entry in the strain tensor. After each small step in the applied strain ($\Delta\gamma = 10^{-4}$), a FIRE minimization algorithm (37) is used to minimize the energy subject to the constraint that the box shape is held fixed (ensuring, therefore, that the strain tensor is defined by a single scalar, the shear strain). Therefore, AQS is equivalent to dynamics in the limit of zero strain rate—where the material is sheared more slowly than any process or relaxation rate inside the material.

To facilitate comparison with the AQRD protocol described in the next section we emphasize that, in linear response and neglecting the effect of particle–particle interactions, shearing the boundary a distance γL_y along the x direction is equivalent to displacing particles in the x direction with a magnitude determined via the height of the system as given by $u_i^\alpha = \gamma \delta^{\alpha x}(y_i - L_y/2)$. Here y_i is the y coordinate of particle i, L_y is the length of the box in the y direction, and δ is the Kronecker delta function of x and dimensional index α (30). An example of such a displacement field is shown in Fig. 1*A*. The overall magnitude of this displacement vector field by an applied strain γ is then given by $|u(\gamma)| = \gamma \left[\sum_i (y_i - L_y/2)^2\right]^{1/2}$. If we assume a uniform distribution of y-coordinate values, as one expects in an amorphous sample, the average magnitude is $|u(\gamma)| \approx \gamma L_y \sqrt{N/12}$. Therefore, an applied shear strain of γ is equivalent to moving a distance $\gamma L_y \sqrt{N/12}$ along a normalized vector field, independent of dimension.

Athermal Quasistatic Random Displacements. Similar to AQS, the system is initialized into a mechanically stable state at the bottom of a potential energy well with energy U and Nd-dimensional

Morse et al.
A direct link between active matter and sheared granular systems

PNAS | 3 of 9
https://doi.org/10.1073/pnas.2019909118

position vector $|x^{min}\rangle$. The system is then displaced along an Nd-dimensional unitless vector $|c\rangle$ with elements c_i and $\langle c|c\rangle = 1$. We explore different methods for choosing $|c\rangle$ described below. First, we define the random strain $\tilde{\gamma}$ of a scalar displacement $\tilde{u}$ along the vector $|c\rangle$ as

$$\tilde{\gamma} = \frac{\tilde{u}}{L_y \sqrt{\frac{N}{12}}}. \qquad [2]$$

This definition ensures that strains (γ) in AQS can be directly compared to random-force strains ($\tilde{\gamma}$) in AQRD, where both are unitless.

Starting from positions $|x^{min}\rangle$ and displacing by an amount $\tilde{u}$, new positions are then $|x\rangle = |x^{min}\rangle + \tilde{u}|c\rangle$, but they are not in a local energy minimum with respect to the reaction coordinates. Therefore, we must evolve the system using a constrained minimization that imposes an external force $|F^{ext}\rangle = -\lambda|c\rangle$, where λ is the Lagrange multiplier, which prevents any motion along $|c\rangle$.

We calculate how such displacements induce changes to the internal stress of the system, in direct analogy to stress–strain curves for AQS. The stress induced by the field $\tilde{\gamma}$ is given by

$$\tilde{\sigma} = \frac{1}{A}\frac{dU}{d\tilde{\gamma}} = \frac{1}{A}\sum_{i=1}^{N}\left(\frac{\partial U}{\partial x_i^{\|}}\frac{dx_i^{\|}}{d\tilde{\gamma}} + \frac{\partial U}{\partial x_i^{\perp}}\frac{dx_i^{\perp}}{d\tilde{\gamma}}\right), \qquad [3]$$

where $A = L_x L_y$ is the area, and we have split the particle motion $\mathbf{x}_i$ into components which are parallel or perpendicular to $\mathbf{c}_i$ as $x_i^{\|}$ and $x_i^{\perp}$, respectively. By definition, $\frac{\partial U}{\partial x_i^{\perp}} = -F_i^{\perp}$ and since we minimize force with respect to the particle position, $F_i^{\perp} = 0$. Thus, the total residual force $\mathbf{F}_i$ on each particle i is parallel to

$\mathbf{c}_i$. Furthermore, we note that $\frac{dx_i^{\|}}{d\tilde{\gamma}} = \mathbf{c}_i L_y \sqrt{\frac{N}{12}}$, resulting in the definition of the random stress

$$\tilde{\sigma} = -\frac{1}{L_x L_y}\sum_{i=1}^{N}\mathbf{F}_i \cdot \mathbf{c}_i L_y \sqrt{\frac{N}{12}} = -\langle F|c\rangle\frac{1}{L_x}\sqrt{\frac{N}{12}}. \qquad [4]$$

This is a generalization of the derivation for shear stress in AQS developed Maloney and Lemaitre (30). Throughout this article, we use variables with a tilde to denote observables that are the AQRD equivalent to AQS counterparts.

In practice, we evolve the system by taking steps of 10^{-4} in the random strain $\tilde{\gamma}$, and after each step we use FIRE minimization (37) to find the constrained local minimum. Thus, instead of applying forces in the FIRE-calculated gradient direction $|F\rangle$, we apply them along $|F\rangle - \langle c|F\rangle|c\rangle$. We impose a stopping condition when every component of the total excess force on every particle is less than a cutoff value of 10^{-14}, set to ensure particle positions to double precision. By construction, there is no drift velocity in the system.

We generate the fields $|c\rangle$ for AQRD using two different methods: one based on random Gaussian fields and another based on plane waves. The Gaussian random fields, which are spatially correlated over a characteristic length scale ξ, are generated using a standard Fourier transform method that respects the periodic boundary conditions. A detailed description is given in *SI Appendix*. Fig. 2 *A–C* illustrates the random vector $|c\rangle$ generated from the correlated Gaussian random field for different correlation lengths $\xi = 1$, 2.5, and 6.25, respectively. To test whether features we observe are dependent only on the correlation length, or whether other features of the field structure are important, we also generate plane-wave-like fields where the x components of the vectors are a sine function of the y coordinate of the particle positions, and the y components of the vectors vanish. For such fields, we define the correlation length
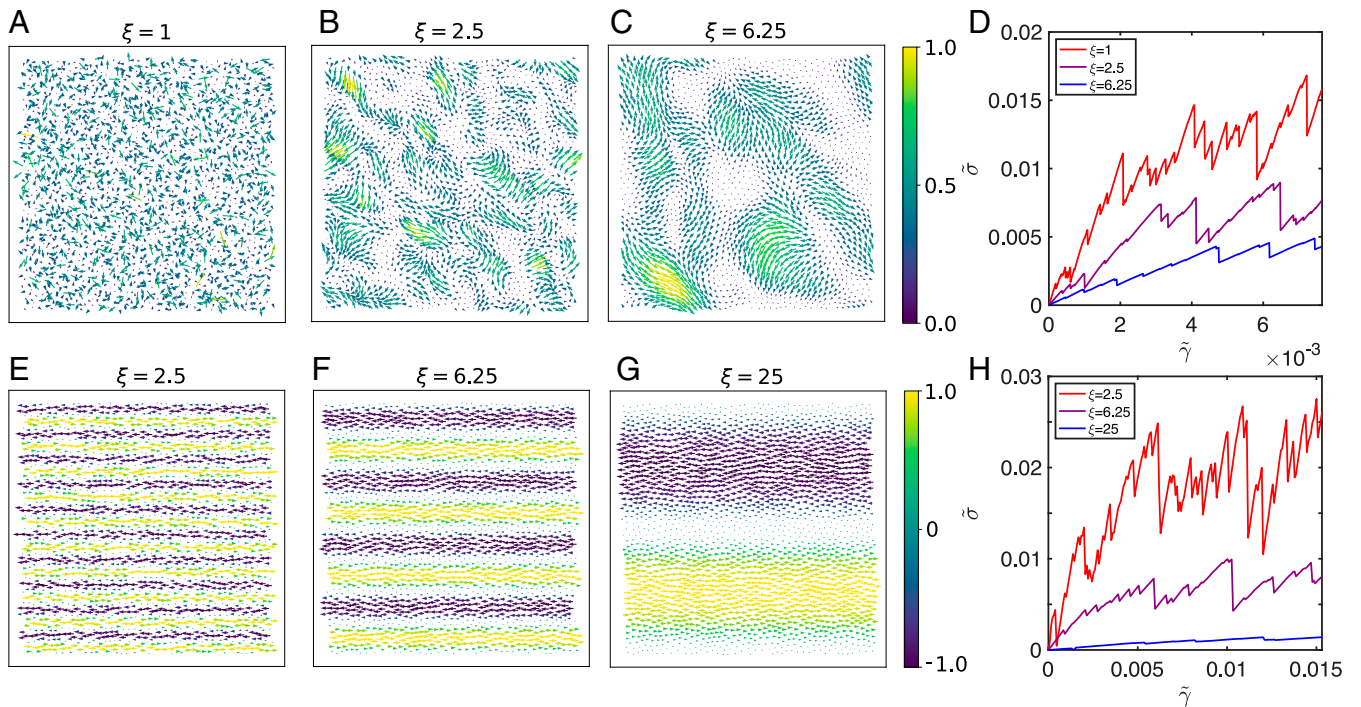

Fig. 2. Effect of random-field correlation length ξ on the mechanical response. (*A–C*) Snapshots of GCFs with correlation lengths (*A*) $\xi = 1$, (*B*) $\xi = 2.5$, and (*C*) $\xi = 6.25$. (*D*) Example random-stress vs. random-strain curves for random fields with different correlation lengths. (*E–G*) Snapshots of WCFs with wave lengths (*E*) $\xi = 2.5$, (*F*) $\xi = 6.25$, and (*G*) $\xi = 25$. (*H*) Example random-stress vs. random-strain curves for wave-like fields with different correlation lengths. In all graphs, we use $N = 2,048$, $\phi = 0.94$, and thus $L_x = L_y = 50.3$.

scale to be half the chosen wavelength. Fig. 2 *E–G* illustrates the random vector $|c\rangle$ generated in a wave-like pattern for different correlation lengths $\xi = 2.5$, 6.25, and 25, respectively. The corresponding displacement field associated with shear under Lees–Edwards boundary conditions is equivalent to a plane wave with a wavelength $2L_y$, which is clear from Fig. 1*A*.

While this version of AQRD applies displacements in a direct analogy to a strain-controlled experiment, we also study a stress-controlled version of random forcing, denoted AQRF, which is an exact limit of standard active matter simulations. Details can be found in *SI Appendix*. Fig. 3 *A–C* compares the dynamics under AQRD (black) and AQRF (red) for a system with the same initial conditions. In linear response (i.e., until the first stress drop in AQRD), the two curves are exactly equivalent. More broadly, until the macroscopic yielding transition (at about 6% strain), stress drops in AQRD are often associated with slip events in AQRF, and the curves still largely follow each other, similar to results in sheared particle systems. Fig 3*D* demonstrates that these similarities persist over a large ensemble. Together, these data indicate that AQRD and AQRF sample similar features of the potential landscape in the preyielding regime, which is also consistent with a full derivation of the mean-field theory (31). This confirms that AQRD is a useful proxy for active matter simulations in the limit of zero rotational noise, and so we focus on AQRD in what follows.

Results

Mean-Field Results. The limit of infinite dimension provides an exact benchmark to investigate properties of structural glasses (14, 39) and has been successfully used, for instance, to study quasistatic shear or compression (8–14). In this framework, we can show that AQS and AQRD are strictly equivalent upon a simple rescaling of the accumulated strain, with a dependence on the correlation length ξ. The full derivation is provided in ref. 31.

To implement a local strain vector $|c\rangle \in \mathbb{R}^{Nd}$ as in AQRD, we assign to each particle a random local strain $\mathbf{c}_i$ drawn from a Gaussian distribution with zero mean defined by

$$\overline{\mathbf{c}_i} = 0, \quad \overline{\mathbf{c}_i \cdot \mathbf{c}_j} = \Xi f_\xi(|\mathbf{r}_{ij}(0)|)/d,$$
$$\text{with} \quad f_\xi(x) = e^{-x^2/(2\xi^2)}/\sqrt{2\pi\xi^2}, \quad \textbf{[5]}$$

where the overline denotes the statistical average over the quenched random strain field, Ξ is a tunable amplitude which has the units of a length (so that the strains remain unitless), and $\mathbf{r}_{ij}(t)$ is the distance between particles i and j at time t (and we focus here on the initial configuration). For simplicity here we have assumed the fluctuations in the field can be described by a normalized Gaussian function with a finite correlation length $\xi > 0$. However, we emphasize that this simplifying condition on $f_\xi(x)$

does not meaningfully affect the main results and the general case is treated in ref. 31. Finally, we include an explicit scaling with dimension d so that the fluctuations in c scale with dimension in the same way as fluctuations in the local strain field in AQS.

In the infinite-dimensional limit, the complex many-body dynamics of pairwise interacting particles become exactly mean field. They can then be reduced to an effective scalar stochastic process for the fluctuating gap between particle pairs, $h_{ij}(t) = d\left(|\mathbf{r}_{ij}(t)|/\ell - 1\right)$, where ℓ is the typical distance between particles and $h_{ij} \sim \mathcal{O}(1)$ (16, 17, 40, 41). To compare the mean-field gap directly with the soft spheres in our simulations, we can use the relationship $h_{ij} = -d\varepsilon_{ij}\frac{\rho_i + \rho_j}{\ell}$. The dynamics are then governed by the distribution of the relative strains $c_{ij} \equiv \|\mathbf{c}_i - \mathbf{c}_j\|$, which are uncorrelated in the limit $d \to \infty$ for distinct pairs of particles (consistent with the mean-field assumption). The variance of a given pair $\overline{c_{ij}^2}$, however, still encodes the spatial correlation of individual local strains, through the quantity

$$\mathfrak{F}(\Xi, \ell, \xi) = d\ell^2 \, \overline{c_{ij}^2} = 2\ell^2 \Xi \left[f_\xi(0) - f_\xi(\ell) \right], \quad \textbf{[6]}$$

which can be straightforwardly computed for a given choice of f_ξ or directly measured in numerical simulations. By adapting the derivation of the mean-field description for shear presented in ref. 16, we find that AQS and AQRD are strictly equivalent in infinite dimension, provided that we rescale the accumulated strain by a factor $\sqrt{\mathfrak{F}}/\ell$, so that it is directly controlled by the variance of relative strains $\overline{c_{ij}^2}$.

For the quasistatic stress–strain curves and the elastic modulus, we specifically predict that the random strain $\tilde{\gamma}$ can be written in terms of the AQS shear strain γ, and therefore the random-displacement stress $\tilde{\sigma}$ and the random-displacement modulus $\tilde{\mu}$ can also be easily scaled as

$$\gamma_{\mathrm{MF}} \equiv \tilde{\gamma}_{\mathrm{MF}} \frac{\sqrt{\mathfrak{F}}}{\ell} \Rightarrow \begin{cases} \sigma_{\mathrm{MF}} = \frac{\ell}{\sqrt{\mathfrak{F}}} \tilde{\sigma}_{\mathrm{MF}}, \\ \mu_{\mathrm{MF}} = \frac{\ell^2}{\mathfrak{F}} \tilde{\mu}_{\mathrm{MF}}, \end{cases} \quad \textbf{[7]}$$

where the MF subscripts emphasize that this is a mean-field prediction, whose validity should be tested in lower dimensions.

We emphasize that the infinite-dimensional calculation predicts that $\mathfrak{F}/\ell^2$ is thus the key quantity to make the AQRD random stress–random strain curves (and other such mean-field observables) collapse onto their AQS counterparts. This quantity is solely prescribed by the statistical features of the input field that we chose to consider. Simply put, $\mathfrak{F}/\ell^2$ is the variance in the strain of the input field—i.e., a measure of the distribution of relative strain between particles—and it completely governs the dynamics of the system.
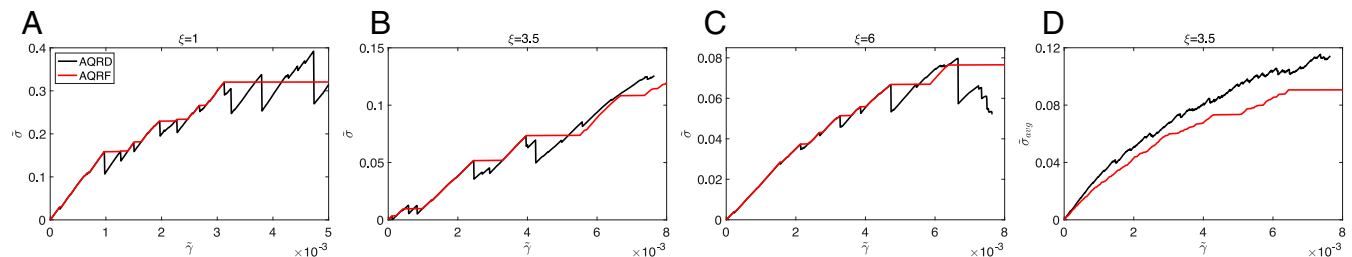

Fig. 3. Comparison of AQRD and AQRF sampling mechanisms. Three generic sample systems with $N = 2{,}048$ and $\phi = 0.94$ are generated and then perturbed by a GCF $|c\rangle$ with (*A*) $\xi = 1$, (*B*) $\xi = 3.5$, and (*C*) $\xi = 6$. The driving mechanism is varied between AQRD—in direct analogy to a strain-controlled measurement—and AQRF—in direct analogy to a stress-controlled measurement. In linear response, the curves are exactly equivalent, but while AQRD systems experience stress drops, AQRF measurements are punctuated by slip events, wherein the system rearranges until it can support the applied stress. As such, in AQRF, the system does not sample local minima in the energy landscape. (*D*) Nevertheless, the curves can be averaged (in this case, over 30 realizations) to give the bulk response. In the preyielding regime, we see that the average response is the same, indicating that both mechanisms sample similar features of the energy landscape.

Under our assumption that $f_\xi(x)$ is a normalized Gaussian function as in [5], we can straightforwardly compute $\mathfrak{F}$ from [6]. By Taylor expanding $\mathfrak{F}$ in the limits $\ell/\xi \ll 1$ and $\ell/\xi \gg 1$, and keeping only the leading terms, we predict a cross-over of the elastic modulus ξ dependence depending on the ratio ℓ/ξ, with $\mathfrak{F} \sim 1/\xi$ at $\ell/\xi \gg 1$ and $\mathfrak{F} \sim 1/\xi^3$ at $\ell/\xi \ll 1$ (31). The specific case of global applied shear strain corresponds to the latter case, as ξ is of the order of the system size for shear. In both cases, this implies that the elastic modulus decreases with increasing ξ, as we will demonstrate numerically below. This matches with physical intuition: It is less efficient to deform a glass with more correlated local strains, i.e., with a larger correlation length. The most extreme case is to consider an infinite ξ: If all particles are driven with the same vector $\mathbf{c}_i$, the whole system is simply translated in space and its effective strain is strictly zero, consistent with having no variance of relative strains ($\mathfrak{F} = 0$). In particular, [7] states that in mean field, AQS is a special case of AQRD, with $\mathfrak{F}/\ell^2 = 1$. See *SI Appendix* for a scaling argument in finite dimension supporting this mean-field picture.

Numerical Results for Random Stress vs. Random Strain. We next test the mean-field prediction in numerical simulations in 2D. Our first observation is that AQS and AQRD give rise to qualitatively similar stress–strain and random stress–random strain curves, as highlighted in Fig. 1 *C* and *F*. Elastic branches—where the stress rises linearly with the strain—are punctuated by points where the system crosses a saddle point instability, causing a stress drop and particle rearrangements as the system transitions to a new energy minimum. The magnitude of the stress drop quantifies the size of the rearrangement event.

In AQS, the stress averaged over many such stress drops gradually rises until about 6 to 7% strain, at which point the system yields. After the yielding point, the average stress remains constant as a function of strain. Moreover, the local shear modulus μ, defined as the slope of the stress–strain curve along elastic branches, is significantly different from the macroscopic coarse-grained shear modulus μ_{global}, defined as the ratio of the average stress at yield to the average strain at yield. This observation is directly related to marginal stability (42) and can be qualitatively predicted from infinite-dimensional analytic theory (8–14).

To develop a more quantitative comparison between AQS and AQRD, as predicted in [7], we focus on three metrics that quantify how AQS and AQRD sample phase space in the preyielding regime: 1) the distribution of local shear/random-displacement moduli μ and $\tilde{\mu}$ along elastic branches, 2) the distribution of (random) strain intervals $\Delta\gamma$ and $\Delta\tilde{\gamma}$ between stress drops, and 3) the distribution of (random) stress drop magnitudes $\Delta\sigma$ and $\Delta\tilde{\sigma}$. We use $\langle\Delta\tilde{\gamma}\rangle$ and $\langle\Delta\tilde{\sigma}\rangle$ to denote quantities which are explicitly averaged over all elastic branches in the preyielding regime.

Scaling of Observables with System Size and Pressure. Previous work has analyzed these statistics in AQS as a function of system size N and pressure p (36, 43, 44), as such data help constrain continuum so-called "elasto-plastic" models to predict features of avalanches in granular matter. In addition, the size of a rearrangement provides interesting information about the nonlinear features of the potential energy landscape, as it is one way of quantifying how far the system has to travel from a saddle point to find a nearby local minimum. The size of avalanches in AQS, quantified by the magnitude of the stress drops and other metrics, is known to exhibit power-law scaling with a large-scale cutoff, and the power law has different exponents on either side of the yielding transition (43). In the preyielding regime the average stress drop is well defined and changes in a systematic way with system size and pressure. Previous work by some of us (36) demonstrated that in AQS the average stress drop exhibits two regimes: a finite-size regime when $N^3 p \ll 1$ in which the size of stress drops remains constant and a second regime when

$N^3 p \gg 1$ where the stress drops scale as $\langle\Delta\sigma\rangle \sim \frac{p}{N}$, which is illustrated by the open symbols in Fig. 4*C*.

Therefore, we first study the statistics of stress drops for the simplest choice for the AQRD vector field $|c\rangle$—an uncorrelated random field (Gaussian correlated field [GCF] with $\xi = 1$), which is also most similar to typical self-propelled particle simulations for active matter. The closed symbols in Fig. 4*C* correspond to stress drop statistics in the preyielding regime for an ensemble of 50 different initial configurations at each value of N and p, showing that precisely the same scaling is seen in AQRD. This highlights that the zero-pressure limit of the avalanche statistics under AQRD is singular, just as in AQS. Although the scaling is identical, there is clearly a shift in the prefactors, which we return to in the next section.

In addition to the magnitude of the stress drops, the strain between saddle points or rearrangements provides another window into the statistical features of the complex potential energy landscape. Fig. 4*B* clearly shows that the mean strain interval
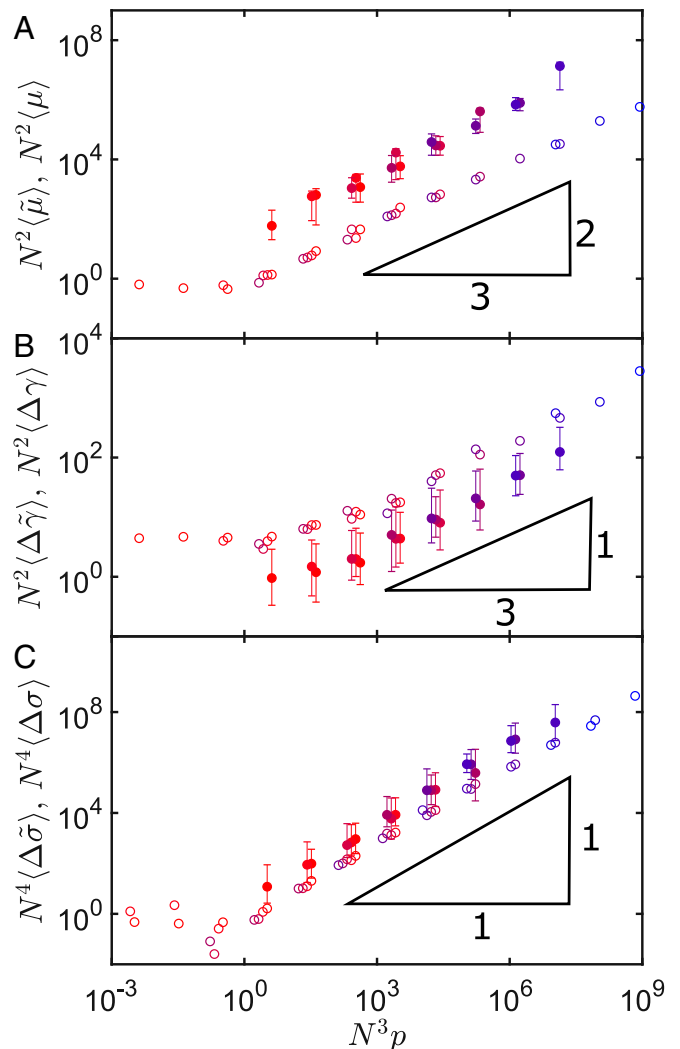

Fig. 4. System size and pressure dependence of landscape statistics. (*A*) Local shear modulus μ. (*B*) Strain distance between rearrangements $\Delta\tilde{\gamma}$. (*C*) Stress drops across rearrangements $\Delta\tilde{\sigma}$ as a function of $N^3 p$ to show collapse with system size and pressure. AQRD with completely uncorrelated random fields is shown with solid circles, while AQS data are shown with open circles. Error bars represent the middle 60% of the distribution and are shown only for AQRD for visual clarity, but are approximately the same for AQS. Colors represent system sizes $N = 64$ (red) and 128, 256, 512, and 1,024 (blue) in an even gradient. Corresponding pressures are $p = 10^{-2}$, 10^{-3}, and 10^{-4}.

between rearrangements scales as $\langle\Delta\tilde{\gamma}\rangle \sim \frac{p^{1/3}}{N}$ in both AQS (open circles) and AQRD (closed circles). Additionally, we measure the average shear modulus between rearrangements, which scales as $\langle\mu\rangle \sim p^{2/3}$ for both AQS and AQRD as shown in Fig. 4A.

Effects of Spatially Correlated Forcing. Although the scaling exponents of the previous section are precisely the same under both AQS and AQRD dynamics, it is clear that there is a systematic offset in the prefactors, despite the fact that care was taken to ensure the definition of effective strain in each case is equivalent.

To understand the origin of this difference, we vary the correlation length ξ of the normalized AQRD vector field $|c\rangle$ measured in units of the smaller particle diameter and use GCFs and wave-like correlated fields (WCFs), as described in *Methods* and illustrated in Fig. 2. For these analyses, system size $N = 2{,}048$ and packing fraction $\phi = 0.94$ are fixed and known to be far from the singular limit. These parameters produce $L_x = L_y = \sqrt{\frac{N\pi(1+1.4^2)}{8\phi}} = 50.3$, where 1 and 1.4 are the diameters of the two species of particles.

Examples of $|c\rangle$ for both GCFs and WCFs are shown in Fig. 2. In each case, the random stress vs. random strain curves exhibit qualitatively similar features, with elastic branches punctuated by stress drops. The overall magnitude of the stress scale changes dramatically, where larger stresses are associated with smaller correlation lengths.

To test the prediction of [7], we first investigate the statistics of the local shear modulus, $\tilde{\mu}$, shown for the GCF data in Fig. 5 A, *Inset*. The GCF distributions shifted by the mean $z_{\tilde{\mu}}$ and scaled by the standard deviation do not collapse as shown in the main panel in Fig. 5A. However, the average is well defined for both GCF and WCF datasets and decreases with increasing ξ (Fig. 5B). Specifically, both datasets are consistent with $\tilde{\mu}$ being a power-law function of ξ.

We note that the AQS data point shown by the black diamond (Fig. 5B) falls on both of the lines describing GCF and WCF data, respectively. This must be the case, as the only input field with correlation length equal to the box size that obeys the necessary constraints—namely that the field has zero mean and respects the periodic boundary conditions—is the one corresponding to simple shear (see *SI Appendix*, section 1B for more details). Nevertheless, this observation confirms that shear is a special case of a more generalized response to displacement fields.

Next, we define a new variable, κ, as the initial random-displacement modulus $\tilde{\mu}_0$ normalized by the initial shear modulus μ_0: $\kappa \equiv \tilde{\mu}_0/\mu_0$. We then explicitly test the mean-field prediction for the shear modulus, [7]: $\kappa = \tilde{\mu}_0/\mu_0 = \mathfrak{F}/\ell^2$. To compute these quantities in our simulation data, we follow the prescription of [6], taking

$$\frac{\mathfrak{F}}{\ell^2} = \frac{d}{N_c}\sum_{\langle i,j\rangle}\|\mathbf{c}_i - \mathbf{c}_j\|^2, \qquad [8]$$

where N_c is the total number of contacts, $\langle i,j\rangle$ denotes contacting neighbors, and we approximate ℓ as the average distance between contacting particles. These quantities, calculated for both the Gaussian correlated fields $\mathfrak{F}_{\text{GCF}}$ and the wave-like correlated fields $\mathfrak{F}_{\text{WCF}}$, are shown by the gray and black data points in Fig. 5C, respectively. We also plot the modulus ratio κ as a function of correlation length for both GCF (green) and WCF (magenta) simulations. Although this is a 2D system far from the infinite-dimensional mean-field case, the mean-field predictions are fairly close to the WCF data and also capture the general trend of the GCF data.

However, the mean-field prediction is not in quantitative agreement so that $\mathfrak{F}/\ell^2 \neq \kappa$, suggesting that in low dimensions
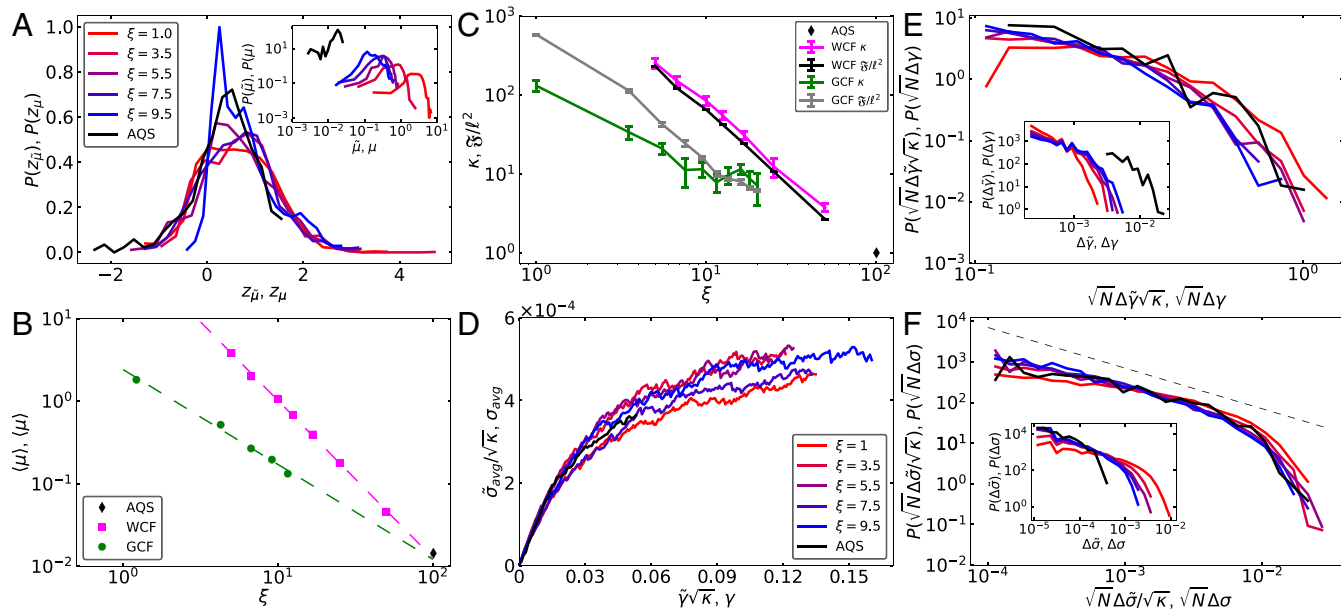
Fig. 5. Collapse of landscape statistics with correlation length. (*A*) Probability distribution of the local effective moduli $\tilde{\mu}$ and μ (*Inset*) and the recentered $z_{\tilde{\mu}}$ and z_μ (rescaled by their standard deviations) in GCF systems with $\xi = 1$ (red) through $\xi = 9.5$ (blue) compared with μ of AQS (black). (*B*) The average effective modulus decreases as a function of correlation length in both WCF and GCF ensembles. All curves approach the AQS value (black diamond), and dashed lines are best fits for $\tilde{\mu}_{\text{WCF}}$ with slope -1.9 (magenta) and $\tilde{\mu}_{\text{GCF}}$ with slope -1.1 (green), respectively, consistent with the mean-field prediction of a slope between -1 and -3. (*C*) A comparison of $\mathfrak{F}/\ell^2$ computed directly via the variance of the field $|c\rangle$ (black and gray lines) and the initial modulus ratio $\kappa = \tilde{\mu}_0/\mu_0$ (magenta and green lines). (*D*) Collapse of average stress–strain curves for GCF random fields onto average AQS stress–strain curve using Eq. 9. Here $\tilde{\sigma}_{\text{avg}}$ and σ_{avg} denote an average over configurations but not all elastic branches. We are additionally able to collapse the distributions of (*E*) the effective strain interval $\sqrt{N}\Delta\tilde{\gamma}\sqrt{\kappa}$ and (*F*) the effective avalanche size $\sqrt{N}\Delta\tilde{\sigma}/\sqrt{\kappa}$, by appropriate scaling of the raw data (*Insets*). Data shown are for GCF, with WCF shown in *SI Appendix*. Additionally, finite-size scaling showing the empirical collapse with the given factors of $\sqrt{N}$ is shown in *SI Appendix*. The avalanche distribution agrees with the reported slope of -1 (dashed black line) (43) given as a guide to the eye.

Morse et al.
A direct link between active matter and sheared granular systems

PNAS | 7 of 9
https://doi.org/10.1073/pnas.2019909118

and in particular at smaller ξ the rescaling of the dynamics cannot be reduced solely to the variance of relative local strains, i.e., from the sole characterization of the input field. Nevertheless, a more general prediction of the mean-field theory is that once the mechanical response at one value ξ is known, all others follow. Thus, one may expect that by using AQS as a reference state we can still collapse low-dimensional simulation data using κ:

$$\sigma \sim \frac{\tilde{\sigma}}{\sqrt{\kappa}}, \qquad \gamma \sim \tilde{\gamma}\sqrt{\kappa}. \qquad [9]$$

For individual response curves, the proper value of κ is defined at $\tilde{\gamma} = 0$ and computed using the response to small AQS and AQRD strains. Averages can then be taken of these individual curves to obtain bulk behavior. Fig. 5 *D–F* demonstrates that the mean-field prediction works remarkably well: Individual stress–strain curves, distributions of strain intervals between stress drops, and the magnitude of stress drops all collapse when properly scaled by κ as predicted by mean-field theory. In addition, the collapsed avalanche data are clearly consistent with the scaling of $P(\Delta\sigma) \sim 1/\Delta\sigma$ reported by Shang et al. (43). This is another indication that bulk responses of AQS and AQRD are controlled by the same physics in that the statistical features of the potential energy landscape are dominated by the scaling of the elastic moduli, i.e., by the curvature of the landscape minima.

This is consistent with observations in Fig. 4; the relative offsets between AQRD curves and AQS curves are κ, $1/\sqrt{\kappa}$, and $\sqrt{\kappa}$ in Fig. 4 *A*, *B*, and *C*, respectively. Furthermore, this gives additional insight that κ remains roughly constant as a function of $N^3 p$.

Effect of Material Preparation and Stability. To this point, we have investigated infinite-temperature–quenched jammed solids, which have a high degree of disorder. Under AQS, such systems exhibit a ductile yielding transition where the preyielding regime transitions smoothly to the postyielding regime with no discontinuity in the stress. It is well known that changing the material preparation protocol alters the disorder in the initial configuration and changes the yielding transition. Recent work using a new swap Monte Carlo algorithm generates ultrastable glasses that are—on the contrary—extremely brittle, with large stress overshoots and discontinuous stress drops at the yielding transition, and data from such simulations strongly suggest that under AQS the yielding transition is in the Random Field Ising Model universality class (45, 46). Although a full study of the nature of the yielding transition in AQRD is beyond the scope of this work, we analyze the random-stress vs. random-strain curves using GCF under different preparation protocols.

The solid lines in Fig. 6 show such curves for different parent preparation temperatures, ranging from $T_{init} = 0.2$ (ductile glass, low stability) to 0.062 (brittle, ultrastable glass, high stability). The dashed curves correspond to the stress–strain response in AQS for the same initial conditions. We observe that in AQRD, the global modulus increases as the stability increases, which is similar to what is observed in AQS. In addition, there is clear stress overshoot (where the average stress increases far above its later steady-state value) for the ultrastable glass, which is similar to what is seen for the yielding transition in AQS, although the yielding transition is much sharper in AQS. Taken together, these results highlight that the qualitative trends for how the yielding transition depends on glass stability are similar in AQS and AQRD and set the stage for future work to study the statistics and spatial structure of the yielding transition in AQRD.

Conclusion

These results demonstrate that shear and random forces perturb disordered solids in remarkably similar ways. In particular, the nonlinear properties of the potential energy landscape traversed by AQS or AQRD display identical scaling exponents.
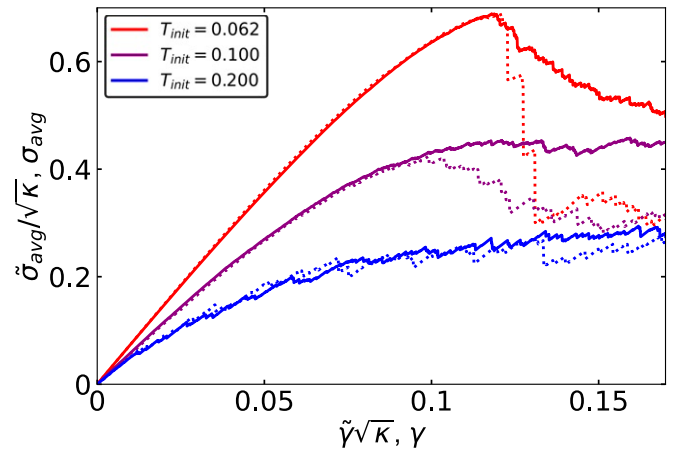

Fig. 6. Average effective stress–strain curves in ultrastable glasses. Stress–strain curves are shown with $\xi = 1$ Gaussian (GCF) driving (solid lines) and AQS driving (dotted lines) on systems which have been prepared via Monte Carlo swap at $T_{init} = 0.062$ (red), $T_{init} = 0.1$ (purple), and $T_{init} = 0.2$ (blue). As in Fig. 5D, $\tilde{\sigma}_{avg}$ and σ_{avg} denote an average over configurations but not all elastic branches. The curves are collapsed via [9]. We see that for lower preparation temperatures, there is a larger shear modulus and a more pronounced peak, in accordance with AQS simulations (45). Our predictions for the collapse agree well up to the yielding point ($\gamma \approx 0.12$).

We discovered that the prefactors for these scaling laws, which generally characterize the stiffness of the material or the magnitude of the curvature in the potential energy landscape, are a power-law function of the correlation length of the input field of displacements. The exponent ranges from -1 to -3 depending on the detailed implementation of the field, consistent with the predictions of the mean-field theory. Since AQS corresponds to an input field where the correlation length is the size of the periodic box, it is not special, but instead a terminal point on a family of random fields that can be characterized by their correlation lengths. In general, materials are stiffer in response to fields with smaller correlation lengths. Conversely, it is more efficient to make a material yield by deforming it in a less correlated way.

Since in the preyielding regime AQRD and AQRF generate nearly identical dynamics—and AQRF is equivalent to self-propelled particle dynamics in the limit where rotational noise is taken to zero first, and then the self-propelled velocity field is taken to zero—these results have important implications for the emerging field of dense active matter. First, they establish that there is a direct equivalence between sheared and active matter systems in this limit, meaning that decades of work on sheared granular matter can be directly imported to understand active systems. Second, they strongly suggest that the dynamics of dense active matter systems could be predicted using tools already developed for sheared granular systems, such as structural and vibrational mode analyses (47). Aspects of such a framework for active matter have already been advanced for instance by Henkes et al. (4, 5). An interesting avenue for future research will be to study how small but finite particle velocities introduce fluctuations into the system that perturb this equivalence to shear. Does this create features analogous to those in finite strain-rate shear simulations? Additionally, we could introduce small but finite magnitudes of rotational noise so that the input displacement fields rotate over time, instead of remaining fixed indefinitely as presented here. We speculate that such dynamics could also be very similar to sheared systems at finite strain rates and/or in the presence of perturbative thermal noise, another active area of research in the rheology community. In experiments, it should be possible to quantify the random stress we define here by studying active photoelastic disks where the internal stress in the system can be inferred from light patterns.

8 of 9 | PNAS
https://doi.org/10.1073/pnas.2019909118

Morse et al.
A direct link between active matter and sheared granular systems

A second obvious avenue for future work is to understand the spatial structure and the nature of the yielding transition under AQRD. Our work confirms that the basic phenomenology is the same: There is a yielding transition where the macroscopic rheology of the material switches from elastic (stress proportional to strain) to fluid-like (stress independent of strain), the macroscopic modulus of the material before it yields is different from the local modulus along elastic branches, and the nature of the yielding transition changes as a function of material preparation. However, this opens more questions than it answers, such as, What are the correlation lengths of the output particle displacement fields that occur in response to the input displacement fields we study? An emerging body of work has begun to show that such correlations tend to long range and depend on the distance to an instability (5, 26), making any relationship to the input field nontrivial. Is the yielding transition under AQRD still in the Random Field Ising Model universality class? Under AQS, brittle glasses fail via localized shear band where all of the strain is accommodated in a small region of the material—Is something similar true in AQRD? Do we have to redefine "localized" to account for the fact that there is no macroscopic symmetry for AQRD with random Gaussian input fields? Does localization depend on the correlation length of the input field? Such questions are more than academic, as they help us to predict how dense materials composed of active matter flow and fail. Answering them will help us to harness the activity of active matter to develop actuated solids that can perform tasks or even predict emergent collective phenomena in crowded active matter systems.

Materials and Methods

Simulations were performed using pyCudaPack (https://github.com/SimonsGlass/pyCudaPacking/) and monteCarloPack (https://github.com/SimonsGlass/monteCarloPCP/), which are available upon request.

Data Availability. Datasets and generating code for this work have been archived and can be accessed at the Duke Digital Repository (https://doi.org/10.7924/r4cv4kb23).

1. V. Narayan, S. Ramaswamy, N. Menon, Long-lived giant number fluctuations in a swarming granular nematic. *Science* **317**, 105–108 (2007).
2. M. E. Cates, J. Tailleur, Motility-induced phase separation. *Annu. Rev. Condens. Matter Phys.* **6**, 219–244 (2015).
3. M. C. Marchetti *et al.*, Hydrodynamics of soft active matter. *Rev. Mod. Phys.* **85**, 1143–1189 (2013).
4. S. Henkes, Y. Fily, M. C. Marchetti, Active jamming: Self-propelled soft particles at high density. *Phys. Rev. E* **84**, 040301 (2011).
5. S. Henkes, K. Kostanjevec, J. M. Collinson, R. Sknepnek, E. Bertin, Dense active matter model of motion patterns in confluent cell monolayers. *Nat. Commun.* **11**, 1405 (2020).
6. L. Berthier, J. Kurchan, Non-equilibrium glass transitions in driven and active matter. *Nat. Phys.* **9**, 310–314 (2013).
7. L. Berthier, E. Flenner, G. Szamel, How active forces influence nonequilibrium glass transitions. *New J. Phys.* **19**, 125006 (2017).
8. C. Rainone, P. Urbani, H. Yoshino, F. Zamponi, Following the evolution of hard sphere glasses in infinite dimensions under external perturbations: Compression and shear strain. *Phys. Rev. Lett.* **114**, 015701 (2015).
9. G. Biroli, P. Urbani, Breakdown of elasticity in amorphous solids. *Nat. Phys.* **12**, 1130–1133 (2016).
10. C. Rainone, P. Urbani, Following the evolution of glassy states under external perturbations: The full replica symmetry breaking solution. *J. Stat. Mech.* **2016**, 053302 (2016).
11. P. Urbani, F. Zamponi, Shear yielding and shear jamming of dense hard sphere glasses. *Phys. Rev. Lett.* **118**, 038001 (2017).
12. G. Biroli, P. Urbani, Liu-Nagel phase diagrams in infinite dimension. *SciPost Phys.* **4**, 020 (2018).
13. A. Altieri, F. Zamponi, Mean-field stability map of hard-sphere glasses. *Phys. Rev. E* **100**, 032140 (2019).
14. G. Parisi, P. Urbani, F. Zamponi, *Theory of Simple Glasses: Exact Solutions in Infinite Dimensions* (Cambridge University Press, 2020).
15. L. Berthier, J.-L. Barrat, J. Kurchan, A two-time-scale, two-temperature scenario for nonlinear rheology. *Phys. Rev. E* **61**, 5464–5472 (2000).
16. E. Agoritsas, T. Maimbourg, F. Zamponi, Out-of-equilibrium dynamical equations of infinite-dimensional particle systems. II. The anisotropic case under shear strain. *J. Phys. Math. Theor.* **52**, 334001 (2019).
17. E. Agoritsas, T. Maimbourg, F. Zamponi, Out-of-equilibrium dynamical equations of infinite-dimensional particle systems I. The isotropic case. *J. Phys. Math. Theor.* **52**, 144002 (2019).
18. Q. Liao, N. Xu, Criticality of the zero-temperature jamming transition probed by self-propelled particles. *Soft Matter* **14**, 853–860 (2018).
19. Y. Fily, S. Henkes, M. C. Marchetti, Freezing and phase separation of self-propelled disks. *Soft Matter* **10**, 2132–2140 (2014).
20. S. K. Nandi, N. S. Gov, Effective temperature of active fluids and sheared soft glassy materials. *Eur. Phys. J. E* **41**, 117 (2018).
21. R. Mandal, P. Sollich, Multiple types of aging in active glasses. *Phys. Rev. Lett.* **125**, 218001 (2020).
22. R. Mandal, P. J. Bhuyan, P. Chaudhuri, C. Dasgupta, M. Rao, Extreme active matter at high density. *Nat. Commun.* **11**, 2581 (2020).
23. P. Olsson, S. Teitel, Critical scaling of shear viscosity at the jamming transition. *Phys. Rev. Lett.* **99**, 178001 (2007).
24. A. Ikeda, L. Berthier, P. Sollich, Disentangling glass and jamming physics in the rheology of soft materials. *Soft Matter* **9**, 7669–7683 (2013).
25. D. Bi, J. H. Lopez, J. M. Schwarz, M. L. Manning, A density-independent rigidity transition in biological tissues. *Nat. Phys.* **11**, 1074–1079 (2015).
26. D. Bi, X. Yang, M. C. Marchetti, M. L. Manning, Motility-driven glass and jamming transitions in biological tissues. *Phys. Rev. X* **6**, 021011 (2016).
27. M. Merkel, M. L. Manning, A geometrically controlled rigidity transition in a model for confluent 3D tissues. *New J. Phys.* **20**, 022002 (2018).
28. N. Xu, V. Vitelli, A. J. Liu, S. R. Nagel, Anharmonic and quasi-localized vibrations in jammed solids—modes for mechanical failure. *Europhys. Lett.* **90**, 56001 (2010).
29. D. L. Malandro, D. J. Lacks, Relationships of shear-induced changes in the potential energy landscape to the mechanical properties of ductile glasses. *J. Chem. Phys.* **110**, 4593–4601 (1999).
30. C. E. Maloney, A. Lemaître, Amorphous systems in athermal, quasistatic shear. *Phys. Rev. E* **74**, 016118 (2006).
31. E. Agoritsas, Mean-field dynamics of infinite-dimensional particle systems: Global shear versus random local forcing. arXiv:2009.08944 (18 September 2020).
32. K. A. Dahmen, Y. Ben-Zion, J. T. Uhl, A simple analytic theory for the statistics of avalanches in sheared granular materials. *Nat. Phys.* **7**, 554–557 (2011).
33. N. W. Hayman, L. Ducloué, K. L. Foco, K. E. Daniels, Granular controls on periodicity of stick-slip events: Kinematics and force-chains in an experimental fault. *Pure Appl. Geophys.* **168**, 2239–2257 (2011).
34. C. S. O'Hern, L. E. Silbert, A. J. Liu, S. R. Nagel, Jamming at zero temperature and zero applied stress: The epitome of disorder. *Phys. Rev. E* **68**, 011306 (2003).
35. S. Dagois-Bohy, B. P. Tighe, J. Simon, S. Henkes, M. Van Hecke, Soft-sphere packings at finite pressure but unstable to shear. *Phys. Rev. Lett.* **109**, 095703 (2012).
36. P. Morse, S. Wijtmans, M. Van Deen, M. Van Hecke, M. L. Manning, Differences in plasticity between hard and soft spheres. *Phys. Rev. Res.* **2**, 023179 (2020).
37. E. Bitzek, P. Koskinen, F. Gähler, M. Moseler, P. Gumbsch, Structural relaxation made simple. *Phys. Rev. Lett.* **97**, 170201 (2006).
38. P. K. Morse, E. I. Corwin, Geometric order parameters derived from the Voronoi tessellation show signatures of the jamming transition. *Soft Matter* **12**, 1248–1255 (2016).
39. P. Charbonneau, J. Kurchan, G. Parisi, P. Urbani, F. Zamponi, Fractal free energy landscapes in structural glasses. *Nat. Commun.* **5**, 3725 (2014).
40. T. Maimbourg, J. Kurchan, F. Zamponi, Solution of the dynamics of liquids in the large-dimensional limit. *Phys. Rev. Lett.* **116**, 015902 (2016).
41. G. Szamel, Simple theory for the dynamics of mean-field-like models of glass-forming fluids. *Phys. Rev. Lett.* **119**, 155502 (2017).
42. J. Lin, M. Wyart, Mean-field description of plastic flow in amorphous solids. *Phys. Rev. X* **6**, 011005 (2016).
43. B. Shang, P. Guan, J.-L. Barrat, Elastic avalanches reveal marginal behavior in amorphous solids. *Proc. Natl. Acad. Sci. U.S.A.* **117**, 86–92 (2020).
44. S. Franz, S. Spigler, Mean-field avalanches in jammed spheres. *Phys. Rev. E* **95**, 022139 (2017).
45. M. Ozawa, L. Berthier, G. Biroli, A. Rosso, G. Tarjus, Random critical point separates brittle and ductile yielding transitions in amorphous materials. *Proc. Natl. Acad. Sci. U.S.A.* **115**, 6656–6661 (2018).
46. M. Popović, T. W. J. de Geus, M. Wyart, Elastoplastic description of sudden failure in athermal amorphous materials during quasistatic loading. *Phys. Rev. E* **98**, 040901 (2018).
47. D. Richard *et al.*, Predicting plasticity in disordered solids from structural indicators. *Phys. Rev. Mater.* **4**, 113609 (2020).

PHYSICS

Morse et al.
A direct link between active matter and sheared granular systems

PNAS | 9 of 9
https://doi.org/10.1073/pnas.2019909118